ANALYSIS OF THE UNSTEADY FLOW AROUND A HYDROFOIL AT VARIOUS INCIDENCES

[1]Lei Shi, [1]Annie-Claude.Bayeul-Lainé, [1, 2]Olivier Coutier-Delgosha

[1]Arts et Métiers ParisTech, LMFL, 8 bld Louis XIV, 59046 Lille cedex, France
[2]Virginia Tech, Aerospace & Ocean Engineering, 460 Old Turner street, Blacksburg 24060 VA, USA
Lei.Shi@ensam.eu, Annie-Claude.Bayeul-Laine@ensam.eu, Olivier.Coutier-Delgosha@ensam.eu

Phone: +0787324448, Fax: +0787324448, E-Mail: Lei.Shi@ensam.eu

KEY WORDS

Numerical simulation, instability, vortex shedding, Transition model

ABSTRACT

The oscillating hydrofoils used in underwater propulsion devices often experience large variations of the flow incidence, which favors cavitation at large angle of attack, and therefore a severe degradation of the performance, additional flow instability, and even cavitation erosion. These various phenomena make numerical simulations of the flow around oscillating hydrofoils quite challenging, especially in cases where the laminar-turbulent transition usually occurs when the blade has a high angle of attack. In the present study, the unsteady flow around a stationary Clark-Y hydrofoil is simulated at five fix incidence angles using the Star CCM+ software. The results show that the lift coefficient increases continuously with the incidence angle up to 15°, even after a separation vortex is generated near the trailing edge. Then, as a slight stall occurs at 20°, the lift coefficients obtained with the k-ω SST and SST $\gamma - \overline{Re_{\theta t}}$ *transition models become significantly different, mostly because of the different prediction of laminar to turbulence transition at the hydrofoil leading edge. Under deep stall condition at 25°, the flow is much more complex and the hydrofoil performance decreases dramatically. The lift force predicted by the SST transition model is more periodic than with the SST k-ω model. Although the general vortex evolution predicted by the two turbulence models is similar, the local pressure experiences larger amplitude variations with the k-ω SST model, as can be also observed from the evolution of the lift coefficient.*

1. INTRODUCTION

Many devices operating in propulsion mode or in energy recovery mode are based on complex kinematics of foil motion, which involve large variations of flow incidences on these foils. It results in unusual phenomena, compared with low incidence flows, like major flow detachments and large-scale recirculation areas. Various unsteady effects related to the continuous angle variation, the interactions with the other foils, and the instabilities generated by the vortices created in the flow, have to be considered. As a motivation, many related works have been conducted extensively by many researchers, especially for flapping foils [1-5]. In this process, one of the most well-known consequences, namely dynamics stall, often occurs when the lifting surface is subjected to a quick motion of fluids or changes in the flow direction. At different stages, it is observed that the production and shedding of leading edge vortex (LEV) and trailing edge vortex (TEV) and the interaction between them can result in noticeable changes of the blade loads. In addition, both for static and oscillating foils, one remarkable flow phenomenon is the laminar-turbulence transition, especially for large attack angle, which is triggered by numerous parameters like the turbulence properties upstream from the device, the surface roughness of the foils, and the local pressure gradient. Although the oscillating foils can be applied to many engineering applications, it has been proved that the pure pitching is not an efficient strategy for thrust generation when considering it for propulsion purpose [6].

The influence of kinematic parameters on the power extraction performance has been studied in many previous work and it can be generally summerized as follows: (1) the oscillating frequency $f_c = fc/U_\infty$ is usually in the range 0.1-0.15 to obtain the maximum efficiency [7]; (2) the heaving amplitude h_0 is often set close to the chord length [8-9]; (3) the best value of the phase lag between pitch and heave is often 90° [10-

11]; (4) the effective angle of attack is a key parameter; (5) the location of the pitching axis is often at one third or one quarter chord length from the leading edge. Then, it was observed that the maximal propulsive efficiency coincides with the triggering of the most unstable modes in the wake at an optimal Strouhal number of around 0.3 [12]. This could be explained by the reverse Karman vortex wake configuration, which directly contributes to an efficient thrust production. The other parameters, such as 3D effects, the foil shape and the Reynolds number, also have a significant influence on the power extraction performance. Besides, some other parameters, which could possibly enhance energy extraction, should be also taken into consideration: it includes the non-sinusoidal motion, corrugated foils, structural flexibility and multiple foil configurations. These investigations aim to better understand the biological mechanisms and thus improve the engineering developments.

In hydrofoils used in underwater propulsive system and other hydraulic devices, the local pressure decrease obtained at large incidence also favors cavitation, which implies that the turbulence/cavitation coupling has to be included in the analysis of such flow conditions. These complex flow configurations have received less attention than flows at lower incidence, until now, as well experimentally as numerically. The present study is thus focused on the numerical investigation of these flows. The objective is to characterize the performance variations (lift and drag coefficients) and the physics of the flows on hydrofoils with variable incidence angles, including angles of attack higher than 20°. Unsteady calculations of the flow around a Clark-Y hydrofoil at five fix incidences have been performed to understand the mechanisms of the flow instabilities under stall conditions. A special attention has been paid at the dynamics of vortical flows and the impact on the hydrofoil performance predicted by the original SST *k-ω* model and SST $\gamma - \overline{Re_{\theta t}}$ transition model.

2. NUMERICAL SETUP

2.1 Turbulence modelling

The two-dimensional Reynolds Averaged Navier-Stokes (RANS) equations are solved, using the STAR CCM+ software. The RANS approach is still the primary computational methodology nowadays for the two-dimensional airfoil flows and it has extensive applications in engineering turbulent flows. The *k-ε*, Realizable *k-ε*, and *k-ω* models are tested first, then the *k-ω* SST model, which was shown by by Malhotra et al. [13] to provide a good estimate of stall angle of airfoils at high Reynolds number, is mostly applied in this study. Considering the occurrence of turbulent boundary layer separation, the SST transition model, which has been proved previously to have the capability to capture the transition process [14-15], is also applied at large incidence angles where stall conditions are obtained, and part of the following analysis is focused on the comparisons between the results obtained with the two models.

The equations solved in the original SST *k-ω* turbulence model can be written as follows:

$$\rho\left(\frac{\partial k}{\partial t}+\frac{\partial(u_j k)}{\partial x_j}\right)=\tilde{P}_k-\widetilde{D}_k+\frac{\partial}{\partial x_j}\left((\mu+\sigma_k\mu_t)\frac{\partial k}{\partial x_j}\right) \quad (1)$$

$$\rho\left(\frac{\partial \omega}{\partial t}+\frac{\partial(u_j \omega)}{\partial x_j}\right)=a_1\frac{\rho}{\mu_t}P_t-\beta\rho\omega^2+\frac{\partial}{\partial x_j}\left[(\mu+\sigma_\omega\mu_t)\frac{\partial \omega}{\partial x_j}\right]+2(1-F_1)\frac{\rho\sigma_{\omega 2}}{\omega}\frac{\partial k}{\partial x_j}\frac{\partial \omega}{\partial x_j} \quad (2)$$

Where $\tilde{P}_k=min(P_t,10\beta^*k\omega),\ \widetilde{D}_k=\beta_*\rho k\omega$ (3)

$$P_t=\tau_{ij}\frac{\partial u_i}{\partial x_j},\tau_{ij}=2\mu_t S_{ij}-\frac{2}{3}\rho k\delta_{ij} \quad (4)$$

$$\mu_t=\frac{\rho k}{\omega}\frac{1}{max\left(\frac{1}{a^*},\frac{\left(S_{ij}S_{ij}\right)^2.F_2}{0.31\omega}\right)} \quad (5)$$

with $x_j\ (j=1,2)$ the coordinates, u_j the velocity components, μ and μ_t the molecular and turbulent dynamic viscosities, S_{ij} and τ_{ij} the strain rate and Reynolds stress tensor components, k the turbulent kinetic energy, ω the dissipation rate, ρ the density, F_1 the blending parameter to switch from *k-ω* to *k-ε* outside from the boundary layers, and F_2 the one that guarantees that the shear stress always varies proportionally to k, including in an adverse pressure boundary layer where it would otherwise be overestimated. The other parameters are constants which are set to their default values in the calculations presented hereafter.

In the $\gamma - Re_\theta$ transition model [16], the production term $\tilde{P}_k$ and destruction term $\tilde{D}_k$ in the turbulent kinetic energy equation are modified as follows:

$$\tilde{P}_k = \gamma_{eff}\tilde{P}_k \quad \text{and} \quad \tilde{D}_k = min\left(max\left(\gamma_{eff}, 0.1\right), 1.0\right)\tilde{D}_k \tag{7}$$

The only difference with the original SST model is the use of the effective intermittency γ_{eff} to control the source term in the *k* equation to induce the onset of transition.

2.2 Flow configuration, mesh, and boundary conditions

The non-symmetrical Clark-Y airfoil with a chord length C = 70 mm was used in the following simulations. Experimental data are available at incidences 5° and 8° [17], which enabled to validate the simulation results in these two flow configurations. The Reynolds number $Re = \rho U_\infty C/\mu$ with U_∞ the free-stream velocity, is set to 7×10^5. The computational domain is extended 10*c* upstream from the position of the foil leading edge and 20*c* downstream, as shown in Figure 1a. An incidence angle α is set between the foil centerline and the incoming flow.

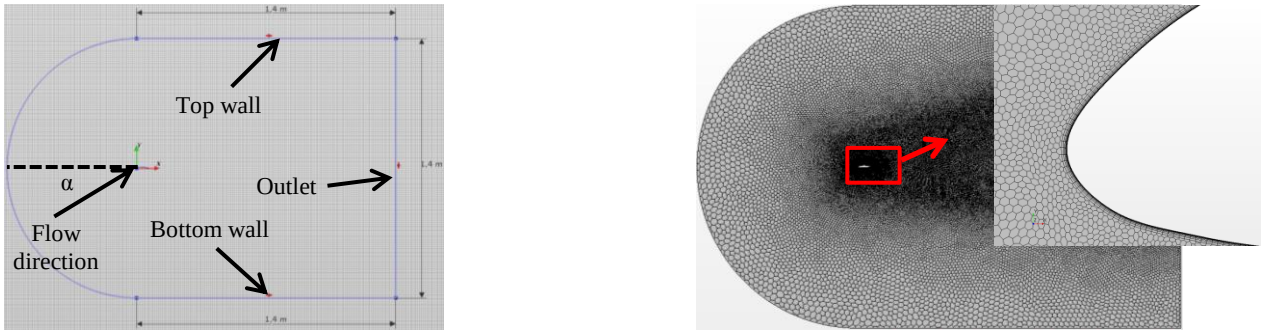

(a) computational configuration (b) mesh for the whole computational domain

Figure 1: Computational domain and mesh generation.

In order to capture the vortex evolution on the hydrofoil suction side and the vortex shedding in the wake at high incidence angles, the mesh is refined close to the foil surface and also in the wake region. An hybrid mesh is used, based on polygonal cells far from the foils and prismatic layers near the foil surface. A constant velocity is applied at the inlet, top and bottom boundaries, and the pressure is set at the outlet. A no-slip wall condition is applied at the foils surface.

Five different meshes with a progressive increase of the refinement (see table 1) are tested and their influence on the lift and drag coefficients at incidences 5° and 8° are indicated in Table 2 and compared to the experimental values. The results show that the lift coefficient is systematically well predicted with meshes 2 to 5, while the relative error on the drag coefficient is significant and almost identical in these four cases.

Mesh	TS (mm)	MS (mm)	GR	NPL	PLT (mm)	TSF (mm)	MSF (mm)	MSC (mm)	NC
Mesh 1	50	0.05	1.3	15	0.5	1	0.5	10	12 671
Mesh 2	10	0.08	1.1	20	0.1	0.5	0.08	6	55 499
Mesh 3	5	0.05	1.04	25	0.1	0.2	0.05	5	122 839
Mesh 4	4	0.02	1.04	25	0.1	0.1	0.02	4	198 662
Mesh 5	3	0.01	1.04	25	0.1	0.08	0.01	4	235 295

Table 1: mesh parameters. The base size of the cells is kept constant for all meshes and equal to 10 mm. TS is the target size at the external boundaries of the domain, MS the minimum size, GR the grow rate, NPL the number of prism layer, PLT the prism layer thickness, TSF the target size on the foil surface, MSF the minimum size on the foil surface in areas of high curvature, MSC the mesh size inside the refinement cone in the wake of the foil, and NC the total number of cells.

Based on these results, the effects of mesh refinement on the quality of the results are still unclear, so in the next section, local comparisons with the experimental velocity profiles will be performed with the five meshes again, in order to clarify which one should be used for the analysis.

5°					8°				
Mesh	C_l	Error	C_d	Error	Mesh	C_l	Error	C_d	Error
Mesh 1	0.810	5.8%	0.0195	18.75%	Mesh 1	1.07233	6.75%	0.02766	25.24%
Mesh 2	0.868	0.93%	0.0152	36.67%	Mesh 2	1.14182	0.71%	0.01938	47.62%
Mesh 3	0.853	0.81%	0.0156	35%	Mesh 3	1.11783	2.80%	0.01976	46.59%
Mesh 4	0.852	0.93%	0.0162	32.5%	Mesh 4	1.12272	2.37%	0.02042	44.81%
Mesh 5	0.853	0.81%	0.0163	32.1%	Mesh 5	1.12562	2.12%	0.02046	44.70%
EXP [17]	0.860	--	0.0240	-	EXP [17]	1.15	-	0.0370	-

Table 2: Time-averaged lift and drag coefficients for different meshes at incidences of 5° and 8°

3. RESULTS AND DISCUSSION

3.1 Validations of different parameters under pre-stall conditions

The influence of several turbulence models on the hydrofoil lift and drag coefficients is shown in table 3. The *k-ε* model under/over-predicts the lift and drag coefficients, while the results obtained with the three other models are almost the same. Since in previous investigations, the SST *k-ω* model was found able to provide accurate prediction of the onset and the amount of flow separation under adverse pressure gradient, and also performed well in the simulation of stall conditions, it is adopted by default in the following test cases.

	Lift coefficient	Error (%)	Drag coefficient	Error (%)
Experiments	0.860	-	0.0240	-
k-ε	0.760	11.6	0.0418	74.2
Realizable *k-ε* two layer	0.853	0.81	0.0170	29.2
k-ω	0.867	0.81	0.0172	28.3
k-ω SST	0.852	0.93	0.0162	32.5

Table 3: Time-averaged lift and drag coefficients obtained with different turbulence models at 5° incidence

Figure 2 displays the streamwise and pitchwise velocities (denoted *U* and *V*, respectively) obtained with the 5 different grids at various locations along the hydrofoil upper surface, using the *k-ω* SST turbulence model. A general good agreement with the experimental data is observed for the two components at all positions. The only significant discrepancy is obtained for the pitchwise compoment at mid chord, from x/C=0.2 to 0.6 (can be seen in figure 2 for x/C=0.4 only). The thickness of the boundary layer at x/C=0.4 and 0.8 looks also slightly overestimated.

Although the mesh refinement does not improve that, it still progressively smoothes the non-physical velocity oscillations that are obtained on the pitchwise velocity. Figure 3 shows the pressure distributions on the foil surface obtained with the 5 grids at a 8° incidence: all numerical results agree well with experiments. Based on these various results, mesh 4 is selected for all next simulations in this study.

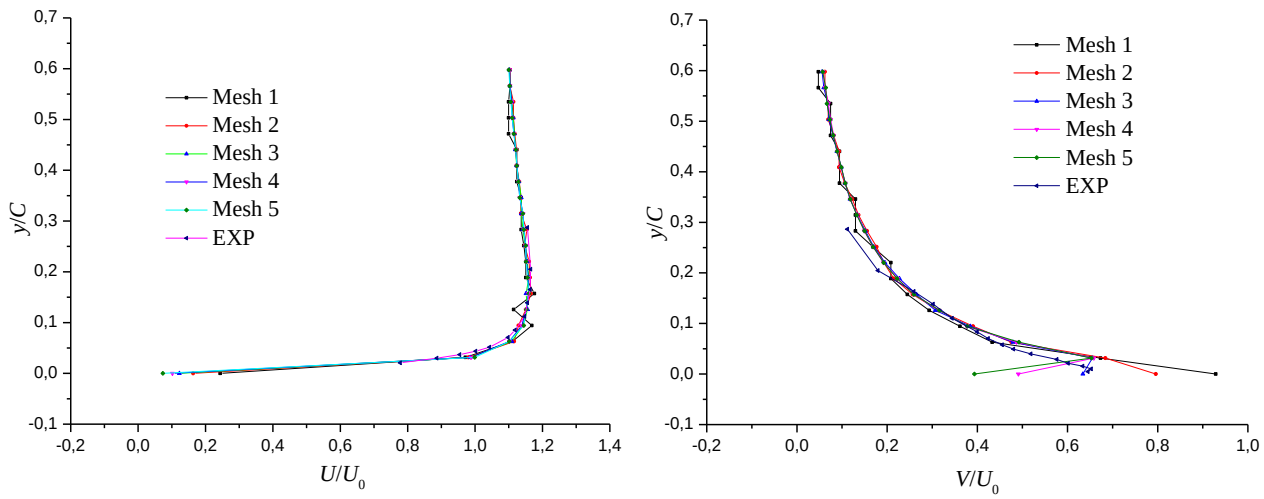

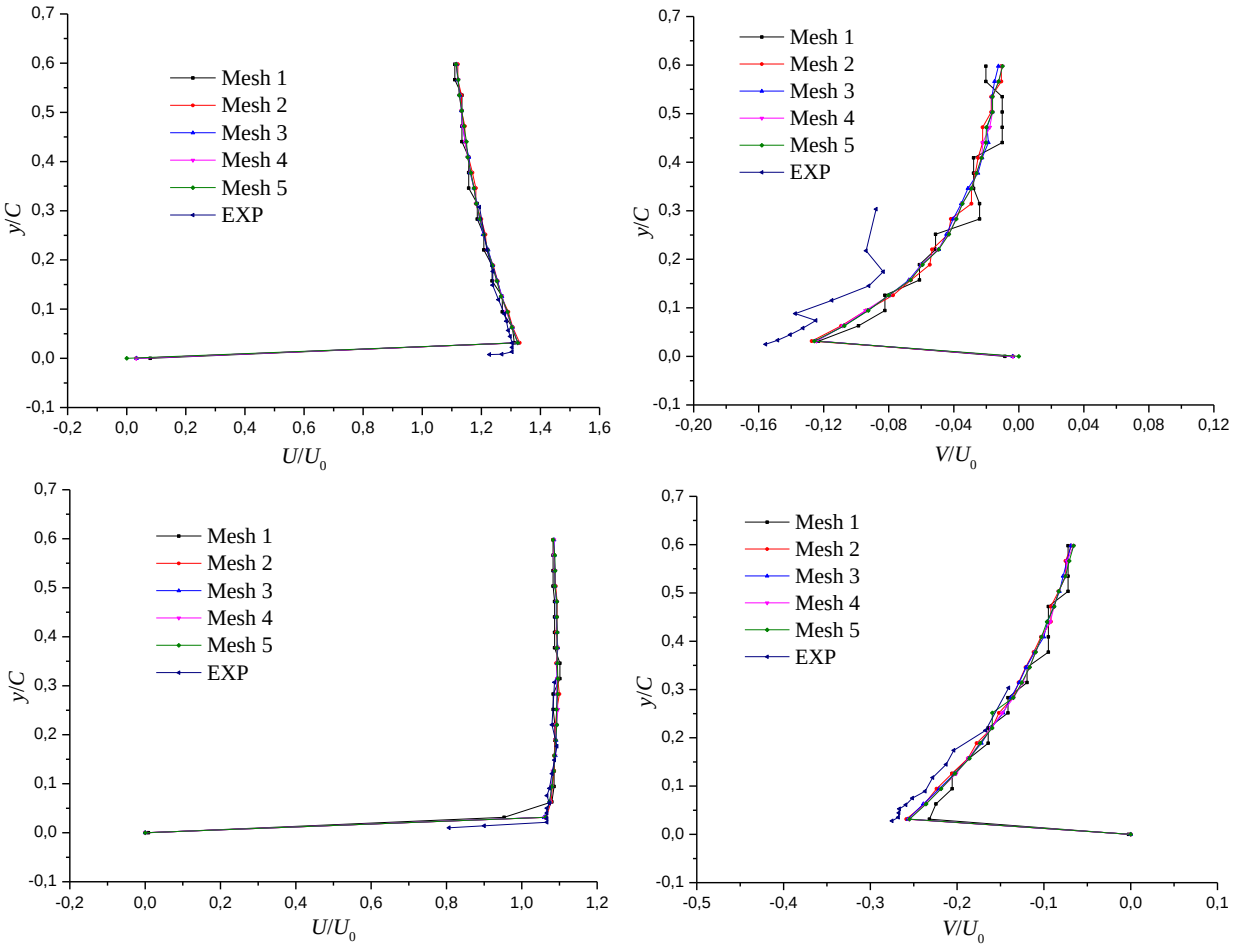

Figure 2: Velocity profiles obtained with the 5 grids for a 5° incidence at positions x/C = 0 (top), 0.4 (middle), and 0.8 (bottom), using the k-ω SST model. The streamwise component is on the left, the pitchwise one on the right.

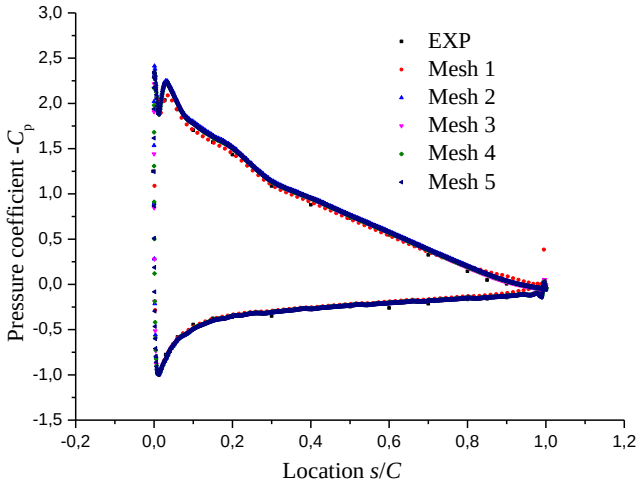

Figure 3: Pressure coefficient distributions for the 5 meshes at incidence of 8°.

3.2 Unsteady flows under slight stall condition

In this section, the flow around the hydrofoil at a 20° incidence is simulated with both the SST k-ω model and the SST transition model (SST TM). As shown in figure 4, the lift coefficient has a periodical time evolution which is directly related to the periodical vortex shedding shown in figure 5. Additional tests were performed to check the required numerical settings to ensure the convergence of all time steps: a convergence level of 10^{-5} with 50 inner iterations and a time-step $\Delta t = 3.5\times10^{-5}$ s are eventually selected. The variations of

lift and drag coefficients obtained by the two turbulence models is shown in Figure 4. The time-averaged lift coefficient at incidence 20° is lower than the one obtained at the 15° incidence (not shown) because of the inception of the stall phenomenon. Besides, the instantaneous lift coefficient predicted by the SST TM model is systematically 4% lower and the period is slightly shorter than the one predicted by the *k-ω* SST model. A much larger difference is observed regarding the average drag coefficient: the value obtained with the transition model is 30% higher than the other one.

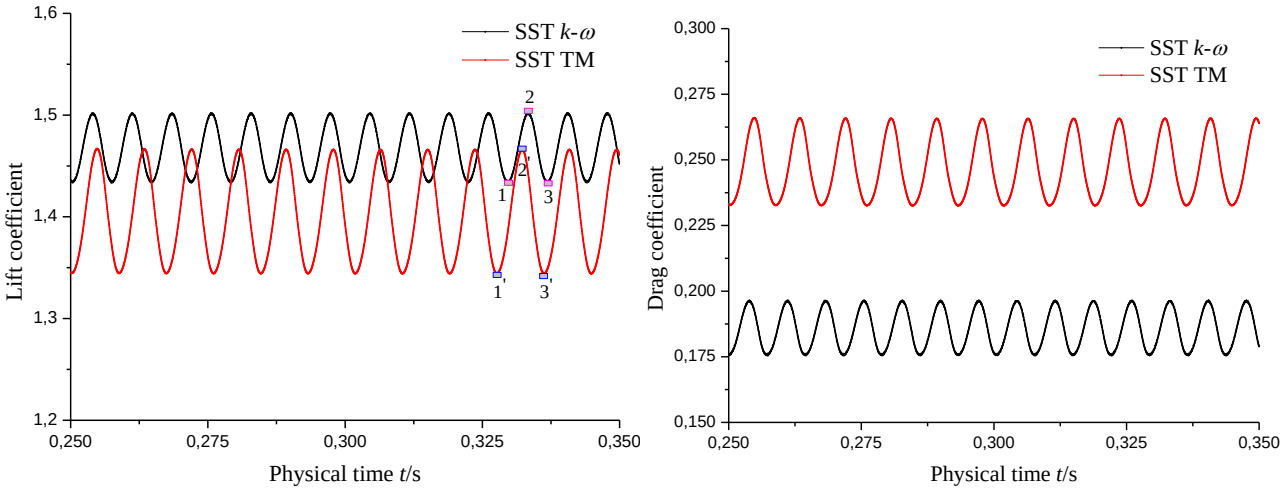

Figure 4: Fluctuations of the lift and drag coefficients at 20° incidence with the *k-ω* SST and the SST TM turbulence models.

A specific cycle of the lift coefficient fluctuation is analyzed in more details in figure 5, to investigate the flow structure evolution and the resulting performance predicted by the two turbulence models. The vorticity contours are plotted at 3 different times denoted 1, 2, 3 in figure 4.

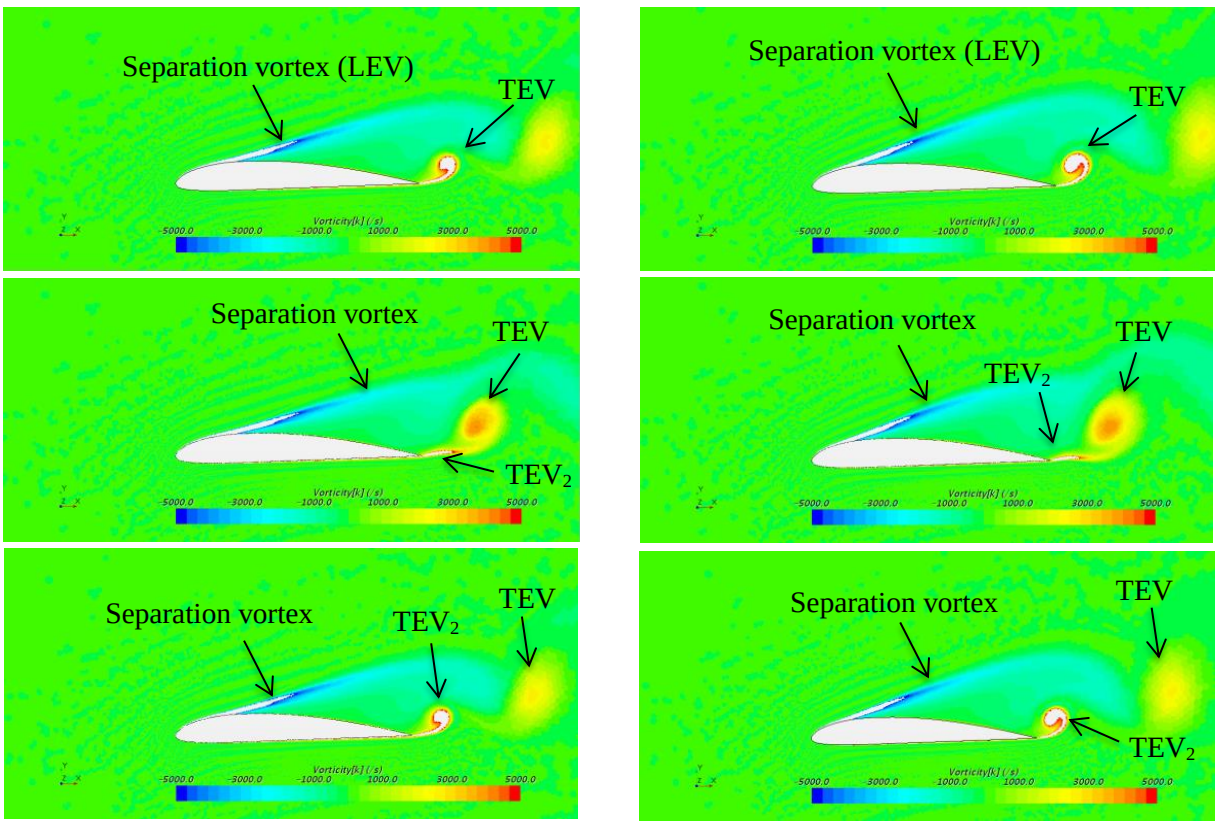

Figure 5: Vorticity contours at times 1, 2, 3 (top to bottom) obtained at incidence 20° with the *k-ω* SST model (left) and the SST TM turbulence model (right).

The flow is mainly characterized by the combination of two vortices, generated by the flow separation at about 20% of the chord, and at the foil trailing edge, respectively. The leading edge vortex (LEV) and trailing edge vortex (TEV) co-exist near the foil trailing edge. At time 1, the magnitude of the LEV is relative low, due to the intense TEV and the load on the upper surface decreases. However, the TEV also induces a decrease of the pressure on the lower surface. As a consequence, the lift coefficient becomes minimal. Afterwards, the TEV detaches from the foil trailing edge and is convected downstream, and a new small-scale secondary TEV_2 is immediately generated. The pressure re-increases on the suction side because of the TEV detachment, combined with the increased negative pressure on the upper surface induced by the strong separation vortex, resulting in the increase of the hydrofoil performance. After that, the influence of TEV_2 results in a decrease of the intensity of the separation vortex, which reduces the load on the suction side. The pressure on the other side also progressively decreases under the influence of the TEV, resulting in a minimal lift at time 3. During this evolution, the pressure change on the suction side mostly depends on the separation vortex, while the pressure evolution on the pressure side is triggered by the TEV. The latter also significantly influences the pressure on the upper surface near the trailing edge.

To investigate the reasons for the different lift coefficient predicted by the two turbulence models, the pressure distribution on the foil surface is displayed in Figure 6. It can be seen that the pressure difference between the pressure and suction sides in the first 20% of the chord is significantly larger with the *k-ω* SST model, at the three different times. It explains the lower lift coefficient obtained with the transition model. To explain this phenomenon, the distribution of turbulent kinetic energy at time 1 is displayed in Figure 7, for the two turbulence models. The results show that transition predicted by SST TM is located more upstream than with the SST *k-ω* model, resulting in a significant difference in the local pressure near the leading edge, since the flow is still attached in one case, and not in the other case.

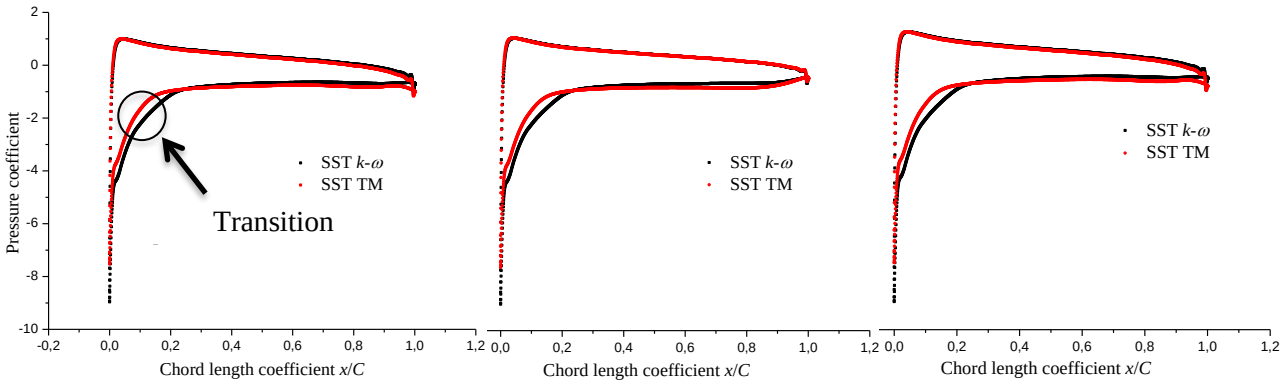

Figure 6: Pressure coefficient on the foil surface at 20° incidence, time 1 to 3 (left to right) with the *k-ω* SST model and the SST TM turbulence model (right)

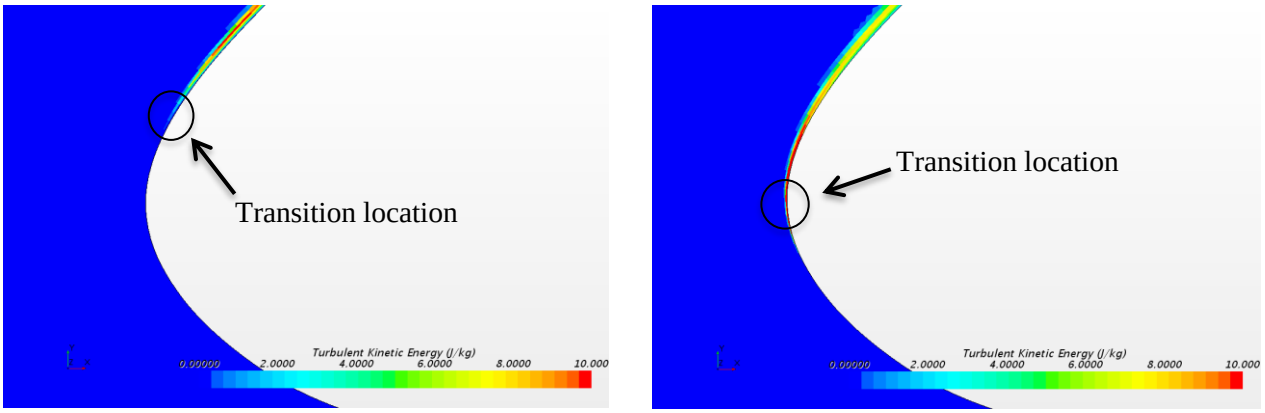

Figure 7: Location of the transition at 20° incidence with the SST *k-ω* model (left) and the SST TM model (right). The colors represent the turbulent kinetic energy.

3.3 Unsteady flows under deep stall condition

To further investigate the stall phenomenon, deep stall conditions are calculated at 25° incidence. Their occurrence coincides with a large decrease of the mean lift coefficient and increase of the drag coefficient. A higher amplitude of oscillations is also observed (see figure 8), which suggests that the flow instability has a stronger influence on the global performance, compared with the previous incidence. Significant differences between the two turbulence models can also be observed regarding the frequency of the oscillations, which is higher with the SST *k-ω*.

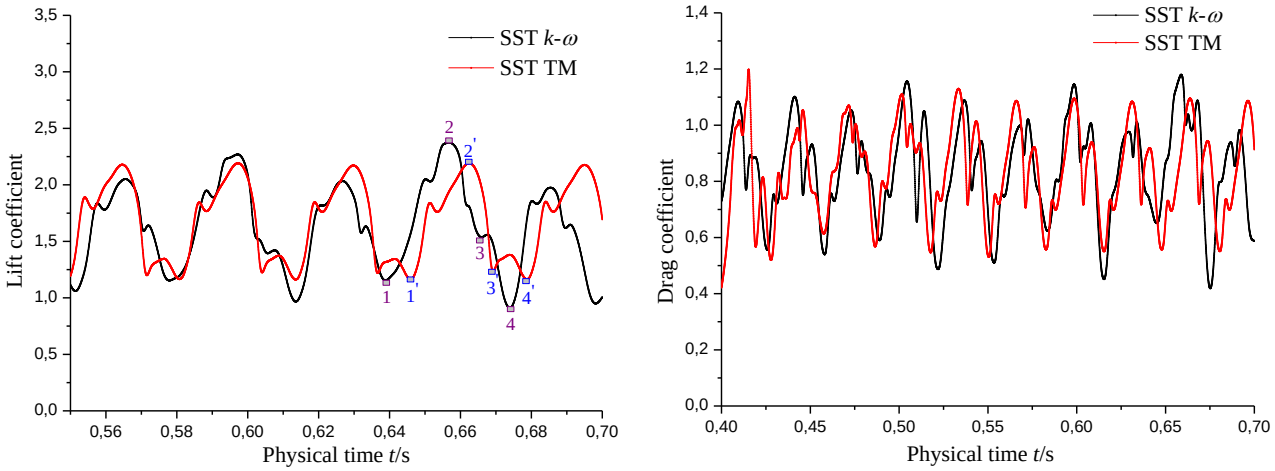

Figure 8: Fluctuation of the lift and drag coefficients predicted by the two turbulence models at 25° incidence.

To analyze the vortex dynamics and its influence on the hydrofoil performance, a specific cycle of the lift coefficient is studied in more details: as indicated in figure 8, time steps 1 to 4 and 1' to 4' are displayed hereafter in figure 9 for the SST *k-ω* and SST TM models, respectively. The 4 time steps are picked at identical stages in the two sets of lift cycles, which results in slightly different physical times.

At time step 1/1' (see Figure 9a), a pair of counter-rotating vortex, denoted "LEV" and "vortex V", are located above the foil upper surface, while a fully developed TEV is also observed at the trailing edge. The intensity of the TEV is higher than the one of vortex V and LEV, which have similar intensities. Between time steps 1/1' and 2/2', the vortex V decays quickly and the TEV is shed downstream from the foil. In the process of LEV migration toward the foil trailing edge, a new secondary vortex structure V_2 is generated in the the shear layer above the foil (see time step 2/2'). During the same time, a secondary TEV_2 is generated and shed immediately between time steps 1/1' and 2/2', followed by the generation of the third TEV_3 (see time step 2/2'). After time step 2/2', the secondary vortex V_2 develops progressively and interacts with the new LEV_2, forming a new pair of counter-rotating vortices that fill a large fraction of the upper surface at time 3/3'. Simultaneously, the size of TEV_3 increases, while it remains attached to the foil trailing edge. Between time steps 3/3' and 4/4', LEV_2 and TEV_3 continue to develop, whereas V_2 and LEV are dissipated. Finally at the end of the cycle, TEV_3 reaches its maximal size and intensity and detaches from the foil trailing edge, while V_2 generates LEV_3 because of the pinch-off phenomenon between LEV_2 and the shear layer, which was also observed in the case of a pure pitching foil [18].

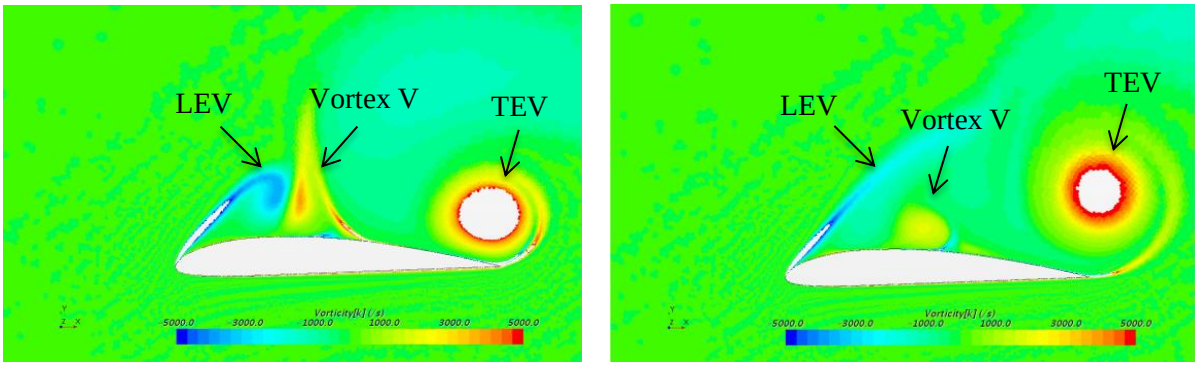

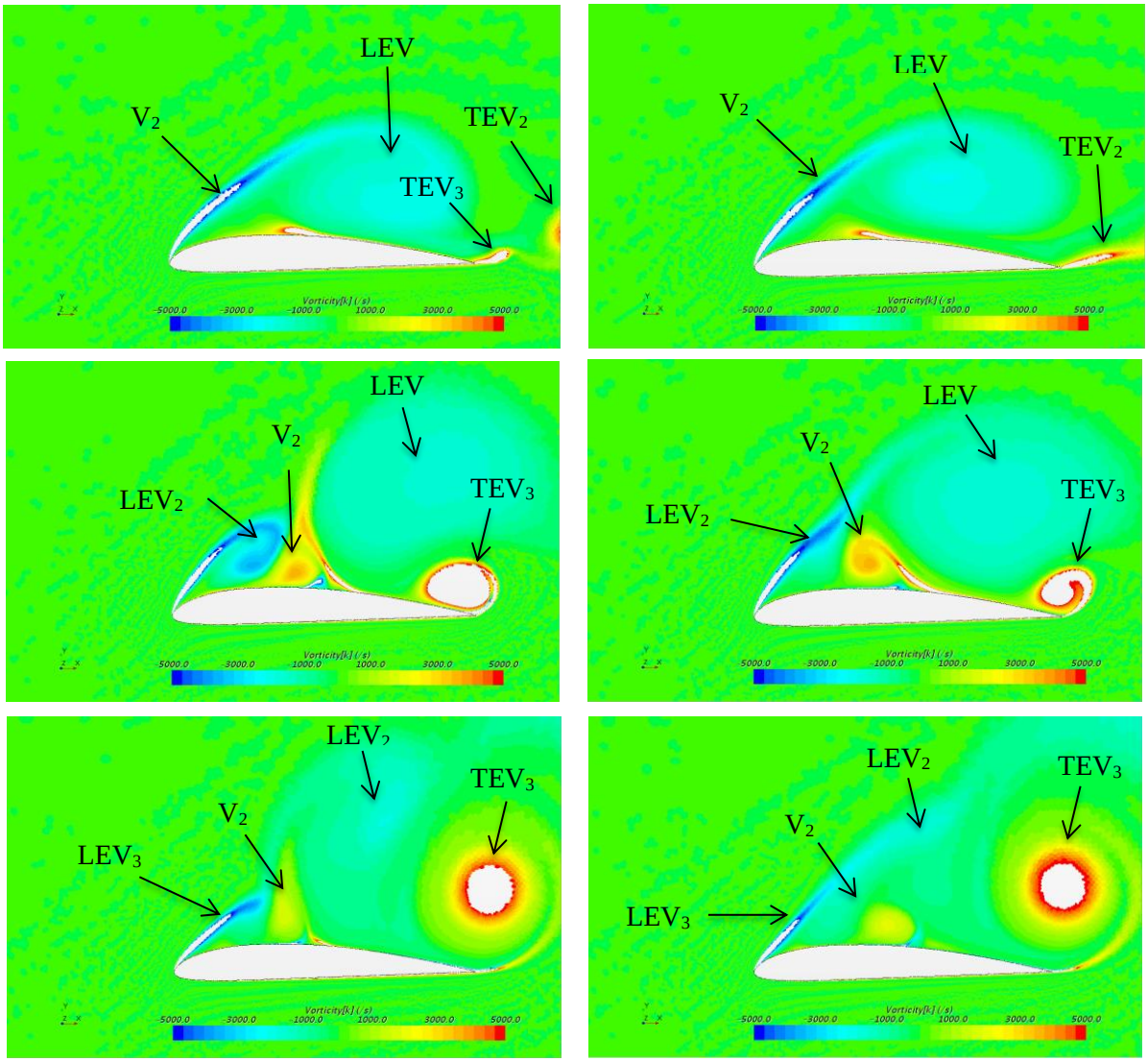

Figure 9: Vorticity contours at times 1 to 4 (top to bottom) obtained with the SST *k-ω* model (left) and the SST TM model (right)

In Figures 10 and 11, the pressure coefficients on the foil surface and the velocity fields at time steps 1 to 4 (and 1' to 4') are plotted for the two turbulence models. It is generally observed that the vortex pattern strongly influences the pressure variations on the foil surface, due to the related local velocity evolution, mostly on the foil suction side.

At time step 1/1', the TEV controls the local pressure on the suction side near the foil trailing edge: a large drop of the local pressure is obtained with the SST *k-ω* model, because it predicts that the vortex is attached to the foil, which in turn induces a large increase of the velocity magnitude in the vicinity of the foil surface. Conversely, this drop is not observed with the transiton model, since the TEV is already detached from the edge, so the velocity is not significantly influenced. However, it can be observed in figure 8 that the lift coefficients are nearly the same at time steps 1 and 1'with the two models. Indeed, vortex V predicted by the SST TM model is larger than with the SST *k-ω* model, which induces a lower pressure at the middle of the foil suction side and eventually compensates the absence of pressure drop at the trailing edge. Conversely, the drag coefficient is significantly lower with the transition model, as it is mostly triggered by the position of the TEV (see time t = 0.64s in figure 8).

At time step 2/2', the lift coefficient has reached its maximum value with both turbulence models, due to the significant pressure decrease on the second half of the suction side, which is related to the local velocity increase induced by the large LEV. This pattern also induces high vertical velocity gradients close to the surface, and thus a simultaneous peak of drag coefficient.

At time step 3/3', TEV_3 has reached almost its maximal growth at the foil trailing edge. It generates a strong overspeed in the rear part of the suction side, which in turn induces a large drop of the surface pressure. Although the vortex intensity is similar in both calculations, its shape and position is slightly different in the two results, which eventually makes the pressure / velocity variations much stronger with the SST *k-ω* model. It explains the notable difference in the lift coefficient, although time steps 3 and 3' are clearly identical stages of the periodical cycle. Finally at time step 4/4', the main vortex structures have detached from the foil surface, which generally smoothes the velocity variations and reduces the foil loading, leading to a minimum lift and drag coefficients in both calculations.

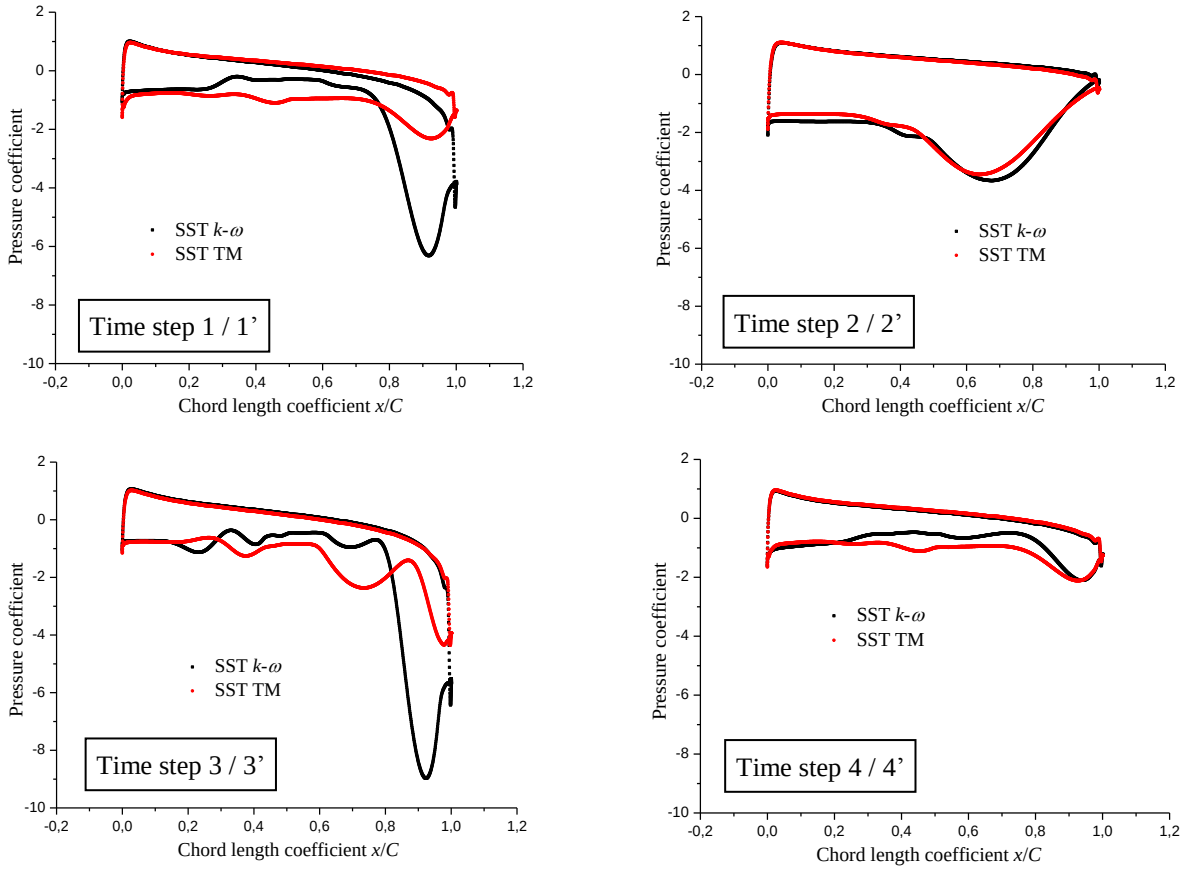

Figure 10: Pressure coefficients on the foil surface for two turbulence models at time steps 1 to 4.

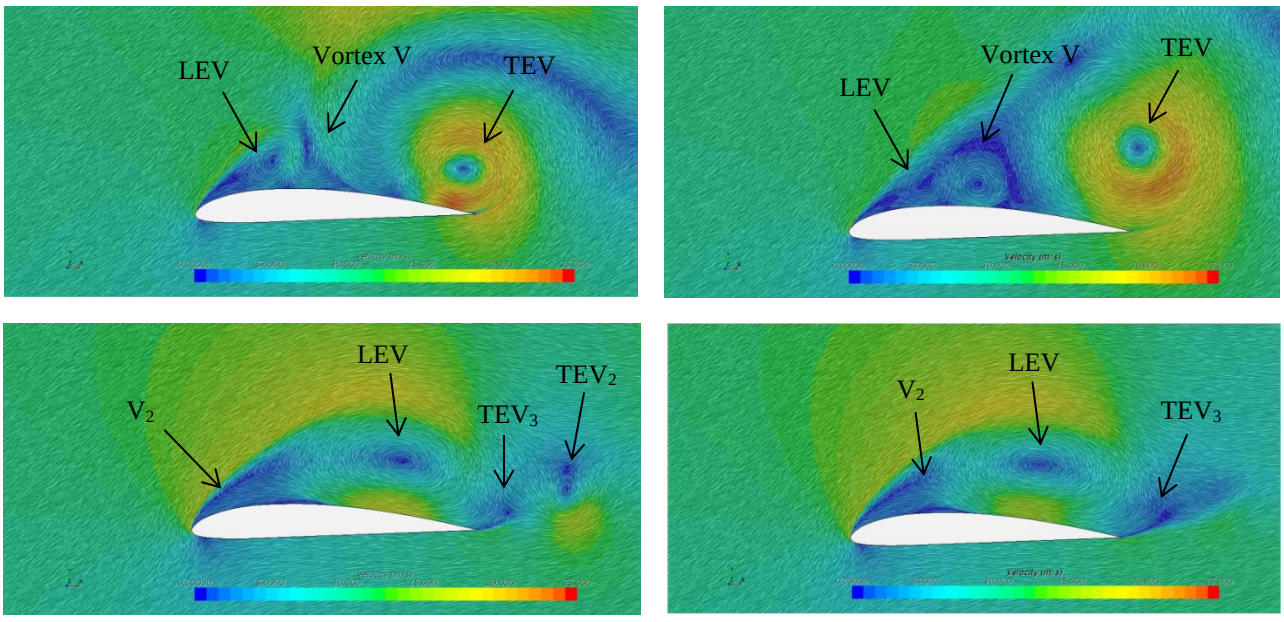

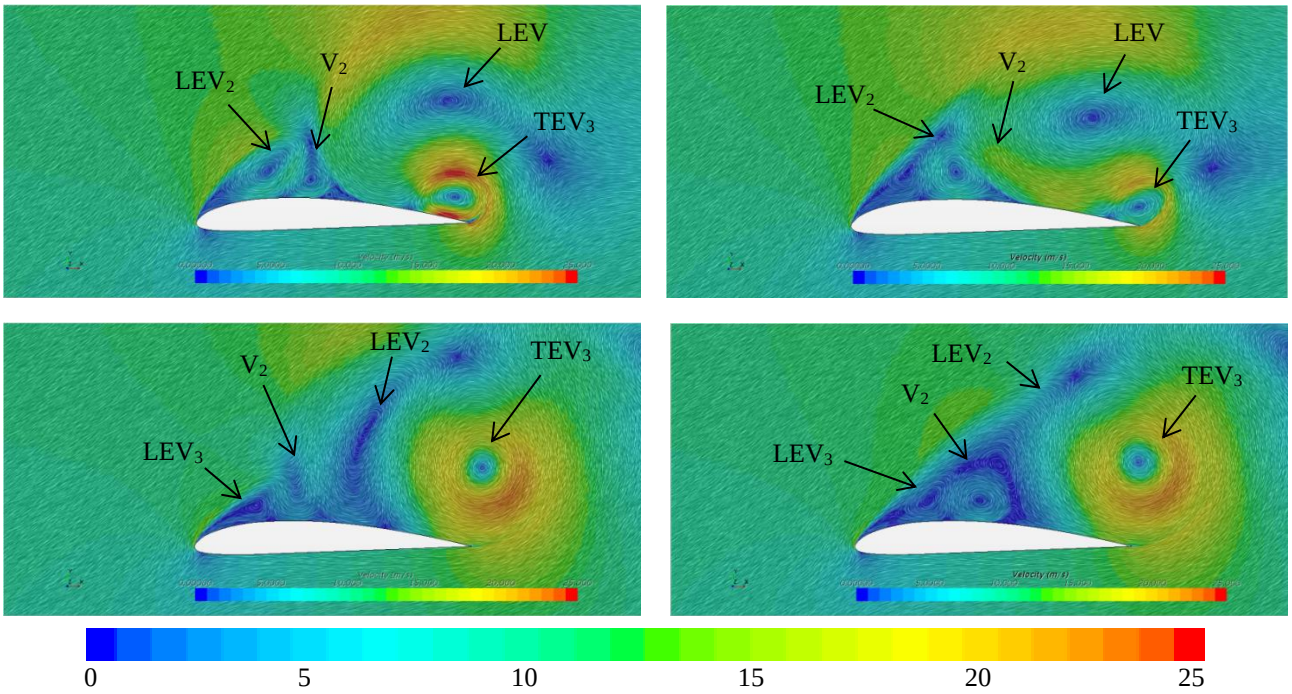

Figure 11: Velocity field obtained with the SST *k-ω* model (left) and the SST TM model (right) at time steps 1 to 4 (top to bottom). The colors indicate the velocity magnitude.

4. CONCLUSION

In the present work, the flow around a stationary Clark-Y hydrofoil was simulated at various incidence angles α. The analysis was mostly focused on the results obtained with the SST *k-ω* and SST TM models, under incipient ($\alpha = 20°$) and developed ($\alpha = 25°$) stall conditions. For such conditions, a detailed study of the vortex evolutions on the foil suction side has been conducted, to explain the time variations of the lift and drag forces. The main conclusions are briefly summarized hereafter:

– Comparisons with the experimental data performed at small angle of attack have revealed a very good agreement regarding pressure coefficient on the foil surface at 8° and the streamwide velocity component at 5° angle, while some discrepancies were obtained for the pitchwise velocity at 5° incidence. However, the smaller order of magnitude of the pitchwise component makes the comparison more challenging.

– For incipient stall conditions at 20° incidence, the periodical evolution of the lift and drag coefficients are strongly related to the dynamics of the vortex due to the boundary layer separation on the suction side, and the trailing edge vortex. The average lift coefficient obtained with the SST *k-ω* model is higher than with the SST TM model: this is a consequence of the significant difference of loading at the hydrofoil leading edge, which is due to the different locations where the transition, and thus the flow separation on the surface, is predicted by the two models.

– Under strong stall conditions at 25° incidence, the blade loading time evolution is controlled by three vortices that are generated on the foil suction side, at the leading edge (LEV), the trailing edge (TEV), and at the location of interaction between the LEV and the shear layer (V). These vortices are mostly responsible for the local pressure variations, between mid-chord and the foil trailing edge. The SST *k-ω* and SST TM models predict slightly different evolutions of the vortices, which in turn induce significant differences in the lift and drag fluctuations. The instant in the cycle where the TEV detaches from the trailing edge, and the maximum size of the vortex V, are two examples of differences between the two models, which eventually change the amplitudes of the lift and drag variations. These differences are likely due to the primary difference between the two model, i.e. the location of the transition at the foil leading edge, which changes the subsequent timeline of vortex growths and interactions. Future work will be focused on the understanding of these mechanisms, to determine which modelling is the most suitable to simulate foils operating at large incidence angles.

REFERENCES

[1] Wang, S., Ingham, D. B., Ma, L., et al. (2010). Numerical investigations on dynamic stall of low Reynolds number flow around oscillating airfoils. *Comput Fluids*, 39, 1529-1541.

[2] Mccroskey, W. J., Carr, L. W., & Mcalister, K. W. (1975). Dynamic stall experiments on oscillating airfoils. *AIAA J*, 14, 57-63.

[3] Leu, T. S., Yu, J. M., Hu, C. C., et al. (2012). Experimental study of free stream turbulent effects on dynamic stall of pitching airfoil by using particle image velocimetry. *Appl Mech Mater*, 225, 103-108.

[4] Sharma, D. M., & Poddar, K. (2013). Investigation of dynamic stall characteristics for flow past an oscillating airfoil at various reduced frequencies by simultaneous PIV and surface pressure measurements. *Proceedings of PIV 13: 10th International Symposium on Particle Image Velocimetry*.

[5] Lee, T., & Gerontakos, P. (2004). Investigation of flow over an oscillating airfoil. *J Fluid Mech*, 512, 313-341.

[6] Mackowski, A. W., & Williamson, C. H. K. (2015). Direct measurement of thrust and efficiency of an airfoil undergoing pure pitching. *J Fluid Mech*, 765, 524-543.

[7] Qiang, Z. (2011). Optimal frequency for flow energy harvesting of a flapping foil. *J Fluid Mech*, 675, 495-517.

[8] Dumas, G., & Kinsey, T. (2006). Eulerian simulations of oscillating airfoils in power extraction regime. *Adv Fluid Mech*, 245-254.

[9] Xiao, Q., Liao, W., Yang, S., et al. (2012). How motion trajectory affects energy extraction performance of a biomimic energy generator with an oscillating foil. *Renew Energy*, 37, 61-75.

[10] Davids, S. T. (1999). A computational and experimental investigation of a flutter generator. Thesis Collection. [11]Mackowski, A. W., & Williamson, C. H. K. (2015). Direct measurement of thrust and efficiency of an airfoil undergoing pure pitching. *J Fluid Mech*, 765, 524-543.

[11] Kinsey, T., Dumas, G., Kinsey, T., et al. (2008). Parametric study of an oscillating airfoil in a power-extraction regime. *AIAA J*, 46, 1318-1330.

[12] Triantafyllou, G. S., Triantafyllou, M. S., & Grosenbaugh, M. A. (1993). Optimal thrust development in oscillating foils with application to fish propulsion. *J Fluids Struct*, 7, 205-224.

[13] Malhotra, A., Gupta, A., & Kumar, P. (2017). Study of static stall characteristics of a NACA 0012 aerofoil using turbulence modeling. *Innovative Design and Development Practices in Aerospace and Automotive Engineering*, Springer Singapore.

[14] Delafin, P. L., Deniset, F., & Astolfi, J. A. (2014). Effect of the laminar separation bubble induced transition on the hydrodynamic performance of a hydrofoil. *Eur J Mech-B/Fluid*, 46, 190-200.

[15] Bartl, J., Sagmo, K. F., Bracchi, T., et al. (2018). Performance of the NREL S826 airfoil at low to moderate Reynolds numbers - A reference experiment for CFD models. *Eur J Mech-B/Fluid*, 75, 180-192.

[16] Menter, F. R., Langtry, R. B., Likki, S. R., et al. (2006). A correlation-based transition model using local variables—Part I: model formulation. *J Turbomach*, 128, 57-67.

[17] Liu, S., Higuchi, J., & Ikohagi, T. (2008). Experimental study of cavity flow behavior on a 2-D hydrofoil. *JSME Int J*, 42, 641-648.

[18] Tseng, C. C. & Hu, H. A. (2015). Flow dynamics of a pitching foil by Eulerian and Lagrangian viewpoints. *AIAA J*, 54, 1-16.